Rapid viscoelastic deformation slows marine ice sheet instability at Pine Island Glacier

S. B. Kachuck[1*], D. F. Martin[2], J. N. Bassis[1], and S. F. Price[3]

[1]Climate and Space Sciences and Engineering, University of Michigan, Ann Arbor, MI, USA
[2]Applied Numerical Algorithms Group, Lawrence Berkeley National Laboratory, Berkeley, CA, USA
[3]Fluid Dynamics and Solid Mechanics Group, Los Alamos National Laboratory, P.O. Box 1663, MS B216, Los Alamos, NM 87545, USA

Key Points:

- We examine the feedback between ice sheet dynamics and solid-earth viscoelastic deformation on grounding line stability
- The viscoelastic response of a low viscosity mantle stabilizes the marine ice sheet instability over decades to centuries
- Viscoelastic uplift on timescales similar to grounding line migration can be a leading term in the feedback ice-sheets/solid-earth

[*]Current address, Climate and Space Research Bldg, 2455 Hayward Street, Ann Arbor, MI 48109 USA

Corresponding author: Samuel Kachuck, skachuck@umich.edu

Abstract

The ice sheets of the Amundsen Sea Embayment (ASE) are vulnerable to the marine ice sheet instability (MISI), which could cause irreversible collapse and raise sea levels by over a meter. The uncertain timing and scale of this collapse depend on the complex interaction between ice, ocean, and bedrock dynamics. The mantle beneath the ASE is likely less viscous ($\sim 10^{18}$ Pa s) than the Earth's average mantle ($\sim 10^{21}$ Pa s). Here we show that an effective equilibrium between Pine Island Glacier's retreat and the response of a weak viscoelastic mantle can reduce ice mass lost by almost 30% over 150 years. Other components of solid-Earth response – purely elastic deformations, geoid perturbations – provide less stability than the viscoelastic response alone. Uncertainties in mantle rheology, topography, and basal melt affect how much stability we expect, if any. Our study indicates the importance of considering viscoelastic uplift during the rapid retreat associated with MISI.

Plain Language Summary

Portions of the West Antarctic Ice Sheet are vulnerable to an instability that could lead to rapid ice sheet collapse, significantly raising sea levels, but the timing and rates of collapse are highly uncertain. In response to such a large-scale loss of overlying ice, viscoelastically deforming mantle material uplifts the surface, alleviating some drivers of unstable ice sheet retreat. While previous studies have focused on the effects mantle deformation has on continental ice dynamics over centuries to millennia, recent seismic observations suggest that the mantle beneath West Antarctica is hot and weak, potentially affecting local glacial dynamics over timescales as short as decades. To measure the importance of viscoelastic uplift in stabilizing grounding line retreat, we coupled a high-resolution ice flow model to a viscoelastically deforming mantle. We find that rapid viscoelastic uplift can reduce the total volume of ice lost over 150 years by 30%, or 18 mm of equivalent sea level rise, making it an essential process to consider when using models to project the future evolution of marine-based ice retreat.

1 Introduction

The West Antarctic Ice Sheet is currently losing around 159±8 Gt/yr of ice, corresponding to a globally averaged sea level rise of about 0.4 mm/yr (Rignot et al., 2008, 2019). Pine Island (Figure 1a) and Thwaites glaciers, which feed into the Amundsen Sea Embayment (ASE), contributed as much as 95 Gt/yr to this total mass flux in 2017 (Rignot et al., 2019). These glaciers are particularly vulnerable to collapse because they have retrograde slopes and are grounded well below sea level (Pattyn, 2018). Such a collapse may already be underway at Thwaites Glacier (Joughin et al., 2014; Waibel et al., 2018) and, although Pine Island may have recently stabilized (Medley et al., 2014; Bamber & Dawson, 2020), it remains at risk for further future unstable retreat. As the catchment area of these and connected glaciers contains ice that would raise globally averaged sea level by 1.2 m (Rignot et al., 2019) and provide a pathway to much larger losses (>2.5 m, Martin et al., 2019), understanding the processes that contribute to (or mitigate) their instability is essential to assessing the impact of future changes.

Marine ice sheets thin toward their edges, and transition into floating ice shelves at a boundary called the grounding line and marine ice sheets on retrograde slopes are vulnerable to the "Marine Ice Sheet Instability" (MISI) (Weertman, 1974; Schoof, 2007, 2012). Several factors may work to stabilize MISI, however, including local buttressing from embayment walls and pinning points (Gudmundsson, 2013) as well as the local sea level change due to solid-Earth and gravity field response to mass redistribution. These latter processes are collectively referred to as Glacial Isostatic Adjustment (GIA) (Gomez et al., 2010, 2012, 2015; Larour et al., 2019; Whitehouse et al., 2019).

We can split GIA into instantaneous components (elastic mantle deformation, changes in the rotational state of the Earth, changes to the gravitational potential) and time-dependent components (viscoelastic mantle deformation and its associated rotational and gravitational perturbations). In a pivotal study, the instantaneous components were identified as a mechanism that can delay—or even stabilize—MISI (Gomez et al., 2010). Larour et al. (2019) recently demonstrated how these instantaneous solid Earth responses to load redistribution can stabilize grounding lines in a continent-wide simulation after 250 years, with significant effects after 350 years.

The timescale of the viscoelastic response is approximately proportional to the viscosity of the mantle (Cathles, 1975; Lingle & Clark, 1985; Bueler et al., 2007), with a strong dependence on the wavelength of the load, as large wavelengths induce deformation in more of the mantle while short wavelengths are more supported by the elastic lithosphere (Figure 1b). Viscoelastic deformation provided only a small feedback to ice loss in Larour et al. (2019) because they focused on longer-term GIA, using a viscosity (6×10^{20} Pa s, Caron et al., 2018) close to the global average viscosity of the top 400 km of the mantle $\sim10^{21}$ Pa s (e.g. Mitrovica & Forte, 1997). This viscosity results in continent-scale viscoelastic relaxation over timescales of thousands of years (Figure 1b, dotted line), though the average viscosity under Antarctica may be closer to 10^{20} Pa s, with slightly shorter timescales (Ivins et al., 2013). The importance of the solid-Earth's viscoelastic response on long-term continental processes is well-reported on with assumed viscosities down to 10^{19} Pa s (Adhikari et al., 2014; Gomez et al., 2015; Konrad et al., 2015; Pollard et al., 2017; Hay et al., 2017; Gomez et al., 2018). Here we investigate the possibility that localized low mantle viscosity could produce bedrock uplift at rates and spatial scales that affect the decadal grounding line retreat observed and projected for the ASE.

The potential for rapid viscoelastic response to mass loss in West Antarctica is due to the presence of a low viscosity upper mantle. Estimates of rheological properties of the subsurface in West Antarctica have typically come from fitting observed and modeled uplift rates to reconstructed ice loads (Simms et al., 2012; Nield et al., 2014; Barletta et al., 2018). Nield et al. (2014) used GPS observations, corrected for elastic uplift, to infer upper mantle viscosities beneath the Antarctic Peninsula as low as 6×10^{17} Pa s with two minima in lithospheric elastic thickness: 20 and 120 km. Using a similar methodology, Barletta et al. (2018) extracted modern viscoelastic rates from GPS time series around the ASE and concluded that the mantle is best represented by a 60 km thick elastic lithosphere overlying a 200 km thick, 4×10^{18} Pa s channel and a 2×10^{19} Pa s half-space (which they call "Best2," cf., Figure 1b, dash-dot). Similarly low-viscosity upper mantles have been inferred in regions geologically analogous to the Antarctic Peninsula, such as Patagonia (Lange et al., 2014) and Southeast Alaska (Larsen et al., 2005), and to the ASE, such as Iceland (Auriac et al., 2013). However, the region is very heterogeneous (An et al., 2015; Ramirez et al., 2016; Hay et al., 2017), requiring high resolution, local constraints on mantle rheology.

We model the dynamic effects of coupling GIA-related deformation to Pine Island Glacier using a sample of upper mantle and lithosphere parameters to investigate the impact of viscoelastic deformation over century time scales. We first describe our method for establishing an upper bound on how much viscoelastic uplift can slow the grounding-line retreat of Pine Island Glacier. We then discuss additional components related to the solid-Earth response, such as perturbations to the geoid and ongoing uplift from past mass loss, and conclude that, though much smaller, these will further contribute to ice sheet stability at the grounding line.

2 Model Setup

2.1 Ice dynamics model

We model the feedback between ice dynamics and GIA-related deformations on Pine Island Glacier by coupling the BISICLES finite-volume adaptive mesh refinement ice flow model (Cornford et al., 2013) to a flat-Earth approximation of the mantle's viscoelastic deformation (Lingle & Clark, 1985; Wolf, 1998; Bueler et al., 2007).

The ice-flow model is forced by a constant accumulation rate (0.3 m/yr) and idealized sub-shelf melt rates M_b proportional to the ice shelf draft H (Cornford et al., 2013; Favier et al., 2014; Waibel et al., 2018):

$$M_b = \begin{cases} 0 & H < 50 \\ (H - 50)/9 \text{ ma}^{-1} & 50 \leq H \leq 500 \text{ m}, \\ 50 & H > 500 \end{cases} \tag{1}$$

chosen to force a rapid but plausible grounding line retreat. We initialize ice flow with basal friction inverted to match present day velocities (Joughin et al., 2009) over the Bedmap2 bedrock topography (Fretwell et al., 2013), as in Cornford et al. (2015). Starting with a uniform 2 km resolution mesh, we allow two levels of factor-of-two mesh refinement, providing a finest resolution of 500 m, necessary for resolving Pine Island Glacier grounding line evolution (Cornford et al., 2016; Larour et al., 2019). While the ice shelf thickness and extent evolve due to sub-shelf melting and grounding line retreat, the calving front is held fixed at its initial location (Γ_{cf} in Figure 1).

2.2 GIA-deformation model

We compute vertical, viscoelastic bedrock velocities in response to mass changes at every timestep using the 2D FFT-based GIA model of Bueler et al. (2007) for one- and two-layer viscous half-spaces overlain by a purely elastic, thin-plate lithosphere. Though this model neglects mantle pre-stress and self-gravitation (Purcell, 1998), these processes are negligible for the response on the domain considered here, with a spatial scale smaller than 1000 km (Wolf, 1998; Klemann et al., 2003).

The Bueler et al. (2007) method updates the Fourier transformed uplift $\hat{U}_{\mathbf{k}}$ (with wavevectors $\mathbf{k}$) at each step using the previously computed uplift and a Fourier transformed load $\hat{L}_{\mathbf{k}}$, which includes ice and seawater. As BISICLES is a finite-volume method, written in terms of fluxes, we use a difference approximation to the bedrock velocity at each timestep of the ice evolution:

$$\dot{\hat{U}}_{\mathbf{k}}^{n+1} = \frac{T\hat{L}_{\mathbf{k}}^{n+1} - \hat{U}_{\mathbf{k}}^{n}}{(\tau + \frac{1}{2}\Delta t)}, \tag{2}$$

where T (m / Pa) is the transfer function (Wolf, 1984; Vermeersen & Sabadini, 1997), relating a load to the deformation at equilibrium, τ (yrs) is an exponential decay constant, and Δt is the BISICLES timestep. We show in supplement S1 how we derive this velocity and how additional modes of viscoelastic deformation can be incorporated.

The deformation of a uniform density, two-layer, incompressible, viscous half-space overlain by an elastic sheet has a time constant τ of

$$\tau = 2T\eta_1|\mathbf{k}|\mathcal{R}, \tag{3}$$

where η_1 is the viscosity of the (infinite) lower layer (see also Bueler et al., 2007, equations 14 and 15). $\mathcal{R} = \mathcal{R}(\eta_2/\eta_1, |\mathbf{k}|h)$ is a function of the ratio of viscosity η_2 of the finite layer and η_1, and the nondimensional thickness of the layer $|\mathbf{k}|h$ (with $\mathcal{R}(1, |\mathbf{k}|h) = 1$, see Equation S5).

The transfer function for this model is given by

$$T = \left(\rho_r g + |\mathbf{k}|^4 \frac{Eh_e^3}{12(1-\nu^2)}\right)^{-1}, \tag{4}$$

for a mantle with density ρ_r and constant gravity g, and a lithosphere with Young's modulus E, Poisson's ratio ν, and effective elastic thickness h_e. The first term in Equation 4 represents hydrostatic equilibrium of the load with mantle deformation. The second term introduces the effect of flexing the lithosphere—supporting some of the load with recoverable elastic stresses and thus limiting the potential viscoelastic response. For small wavelength loads ($|k| \to \infty$), $T \to 0$, indicating no deformation within the mantle and complete elastic support of the load by the lithosphere. The decay time (Eq. 3) and transfer function (Eq. 4) above match the dominant mode of deformation in viscoelastic solutions that employ the correspondence principle (Vermeersen & Sabadini, 1997) (see also Figure S1a,b).

The total deformation includes both the single viscoelastic relaxation mode of Eqs. 3 and 4 and an instantaneous elastic mode. The magnitude of this elastic mode is the response of a homogeneous half-space, with the bulk and shear moduli λ and μ of the lithosphere (Table 1), to a harmonic load with wavenumber k. We remove the elastic flexure component ($\rho_r gT$) already considered in the viscoelastic mode (Kachuck & Cathles, 2019) to obtain:

$$U_{\mathbf{k}}^{\mathrm{el}} = T_{\mathbf{k}}^{\mathrm{el}} \hat{L}_{\mathbf{k}} = \frac{1 - \rho_r gT}{2k} \left(\frac{1}{\mu} + \frac{1}{\lambda + \mu} \right) \hat{L}_{\mathbf{k}}. \tag{5}$$

This expression matches the elastic component of viscoelastic solutions in the range of wavelengths we consider, as shown in Figure S1(d). Including elastic deformation, the total vertical bedrock velocity is

$$\dot{\hat{U}}_{\mathbf{k}}^{n+1} = T^{\mathrm{el}} \frac{\hat{L}_{\mathbf{k}}^{n+1} - \hat{L}_{\mathbf{k}}^{n}}{\Delta t} + \frac{T\hat{L}_{\mathbf{k}}^{n+1} - \hat{U}_{\mathbf{k}}^{n}}{(\tau + \frac{1}{2}\Delta t)}. \tag{6}$$

At the small scales for this problem (< 1000 km), the simplifications associated with our isostatic adjustment model are justified (see Figure S1a-d). However, over longer spatial scales, e.g. those associated with the entire ASE catchment area, these assumptions become increasingly questionable, as variations in the mantle viscosity (both radially and laterally) (Hay et al., 2017), as well as density variations and self-gravitation (Purcell, 1998), become increasingly important.

2.3 Solid Earth structure

We consider representative mantle rheologies to quantify the effects of the coupling between isostatic adjustment and grounding line retreat (see Table 1). For an upper bound on the effect of including the solid-Earth feedback at Pine Island Glacier, and given the large spatial variations in properties in the region, we consider a low viscosity (10^{18} Pa s) half-space with a thin lithosphere (25 km), both on the lower edge of their respective uncertainty ranges (e.g., Simms et al., 2012; Nield et al., 2014, in the Antarctic Peninsula). For insight on the controls of the feedback we compare with thicker lithospheres (60 km and 110 km) and more viscous mantles ("Best2" from Barletta et al. (2018) and the global upper mantle average UM). "Best2" is the only model for which $\mathcal{R}$ in equation 3 is not unity ($\tilde{\eta}_{\mathrm{Best2}} = 0.2$).

3 Results

At the start of the simulation, the ice sheet in the domain loses 40 Gt/yr, concentrated at the grounding line, consistent with observations (Medley et al., 2014, their Fig-

Table 1. Material parameters considered. We use a uniform mantle density of 3313 $\mathrm{kg/m^3}$, and elastic parameters $\lambda = 34.2667$ GPa and $\mu = 26.6$ GPa (Dziewonski & Anderson, 1981). η_2 is the viscosity of the 200 km layer overlaying the halfspace with viscosity η_1. Gravitational parameters are $g = 9.81$ m/s and $G = 6.063 \times 10^{-11}$ N $\mathrm{m^2/kg^2}$.

Model	h_e (km)	η_2 (Pa s)	η_1 (Pa s)
Upper Bound (UB)	25 60 110	1×10^{18}	
"Best2"[a]	60	4×10^{18}	2×10^{19}
Upper Mantle (UM)	60	1×10^{21}	

[a]Barletta et al. (2018)

ure 10). Over the course of 150 years, with static bedrock topography (NoGIA), ice shelf melting drives the ice sheet into accelerated retreat, losing over 300 Gt/yr at the simulation's end (0.83 mm/yr sea level equivalent, SLE), shown by the dashed line in Figure 2(a). When coupled to a low-viscosity mantle and a thin lithosphere (UB) using equation 6, the viscoelastic uplift slows the mass loss, with a final rate of only 170 Gt/yr (0.48 mm/yr). In terms of total mass loss and contribution to sea level (Figure 2b), the simulation predicts a loss of 24,000 Gt over 150 years without GIA-related deformations and 17,000 Gt with them. The response of the mantle thus reduces mass lost from Pine Island Glacier over 150 years by 7,000 Gt (17.5 mm equivalent sea level), or a percentage difference of 30% of total mass lost compared to the uncoupled case (Figure 2c).

In our simulations, an initial period of relaxation from uncertain initial conditions (Favier et al., 2014) causes mass to temporarily collect near the grounding line. This results in an instantaneous elastic subsidence that increases water depth, increases mass loss of the glacier, and is reflected as a negative percentage difference relative to the static bedrock simulation NoGIA. This negative percentage difference, shown in in Figure 2c, is purposefully clipped because it is spuriously large, as the mass lost is small in the first 10 years, and the elastic subsidence is overtaken by viscoelastic uplift in all simulations by 25 years, which reduces cumulative mass lost relative to the static bedrock simulation NoGIA (Figure 2c). By 180 years, the grounding line in the NoGIA simulation has reached the boundary of the domain, and cannot be run further in time.

The Earth's rheology affects the magnitude of the feedback. Increasing the effective elastic thickness of the lithosphere decreases how much viscoelastic deformation occurs in response. Mass lost when coupled to a 60 km lithosphere (and 10^{18} Pa s half-space) is 20% less after 150 years than with static bedrock and is reduced by 10% with a 110 km lithosphere (Figure 2c, solid, grey). Increasing the viscosity delays the bedrock response, reducing the uplift's ability to keep pace with grounding line retreat. The stability from viscoelastic uplift on the inferred ASE rheology "Best2" from Barletta et al. (2018) is more moderate, reducing the total volume lost by 12% over 150 years (Figure 2, dash-dot). A half-space with a viscosity of 10^{21} Pa s provides the least stability of all, only 3%, as shown by the dotted line (Figure 2, dashed).

The stabilized retreat is seen in the evolution of the grounding line in Figure 3(a). After 15 years of slow thinning, the grounding line enters the rift valley (see grey contours in Figure 3(a)) and then rapidly recedes through it, covering almost 250 km over 150 years along a central flow line when uncoupled to any GIA-related deformation (Figure 3b, dashed). Rapid deformation of the low viscosity half-space (UB) slows this retreat, as seen by the time that each model's grounding line reaches the five points i-v in Figure 3 (taken at 25-year increments from the grounding line of the NoGIA simulation), with the coupled grounding line lagging by over 25 years at point v in Figure 3(b).

Retreat is slowed by rapid uplift at the grounding line. Figure 3(c) shows the ice thickness at the grounding line over time. The effect of viscoelastic uplift is highlighted by linking the depth and time that the NoGIA and UB simulations reach the grounding line locations i-v. Early on (point i), the retreats have progressed similarly. By the time the grounding line in model UB has reached point iii (84 years), the solid-Earth has uplifted the surface there by 35 meters resulting in a cumulative delay of 9 years (75 years without GIA coupling). By point v (125 years without GIA coupling, 151 with), the uplift is almost 65 meters.

The snapshots of uplift and uplift rate in Figures 3(d-g) give more regional context. Here we can see that the uplift is highly localized near the grounding line, where the mass loss is concentrated, and far from present GPS observations (dots in Figures 3g). After the grounding line retreats through a given location, thinning of the floating ice does not induce further uplift, concentrating the uplift upstream of the grounding line. As the bedrock deepens inland, this uplift reduces water depth at the grounding line, stabilizing the ice as in Gomez et al. (2010). The time-scale over which this stabilization operates is decadal, given the low subsurface mantle viscosity.

4 Discussion

GIA-related deformations are a significant negative feedback on mass loss in a region characterized by a low viscosity mantle. We have demonstrated how the viscosity of the mantle and elastic thickness of the lithosphere mediate this feedback (Figure 2). We have omitted other components of the solid-Earth response that could affect the dynamics of the grounding line, like the combined gravitational effects of ice mass loss and mantle displacement (Gomez et al., 2010, 2015; Larour et al., 2019) and the ongoing uplift from older mass loss (Barletta et al., 2018). We show below that the effect of these are smaller in magnitude than the viscoelastic uplift. And because of the fast viscoelastic uplift, we see a larger response near the grounding line than the pure elastic results of Larour et al. (2019) over centennial timescales. The negative feedback modeled here is sensitive to a balance between the speed of uplift and the rate of grounding-line retreat, which we show below is sensitive to the bedrock topography and basal melt rate. These other processes then require further constraints to establish the expected importance of GIA as a stabilizing process in this region.

4.1 Gravitational and Elastic Effects

Ice sheet mass loss leads to local reductions in gravitational attraction at the Earth's surface, which in turn leads to a lowering of sea level at, and a stabilization of, a retreating grounding line. This perturbation to the geoid from ice mass loss is counterbalanced somewhat by the gravitational attraction of mantle material as it uplifts. Gomez et al. (2015) showed that the total perturbation of the geoid can be almost as stabilizing as the deformable solid surface for simulations of the whole Antarctic continent over thousands of years. Larour et al. (2019), on the other hand, demonstrated that perturbations to the geoid were smaller than purely elastic effects for continent-scale simulations on timescales of several hundred years. We show that both elastic and geoid effects are smaller than rapid viscoelastic uplift.

We estimate the effect of the instantaneous elastic component by simulating the feedback with viscoelastic deformation only (equation 2) and compare the mass lost over time with the total deformation model (viscoelastic + elastic, equation 6). After about 10 years of spuriously large effect, due to an initial elastic subsidence at the grounding line as described earlier, the elastic component contributes less that 2% to the total feedback on mass lost over 150 years from deformation in models UB, Best2, and UM (see Figure S2).

To estimate the magnitude of the effect of changes in the geoid (from ice, sea-water, and mantle mass redistribution), we use the gravitational potential of a harmonic surface mass density σ with wavenumber k given by (Fjeldskaar, 1991)

$$\Phi_{\mathbf{k}} = \frac{4\pi G \hat{\sigma}_{\mathbf{k}}}{kg}. \tag{7}$$

The surface mass density perturbation is a combination of the ice load (above flotation) and the vertically deformed mantle material

$$\hat{\sigma}_{\mathbf{k}} = \hat{L}_{\mathbf{k}}/g + \rho_r \hat{U}_{\mathbf{k}}. \tag{8}$$

Over the small region we consider, we can treat the effect of a rise in the geoid as a lowering of the bedrock and vice versa, as these have the same effect on the local sea level at the grounding line. The geoidal sea level calculated using the modeled ice thicknesses from model UB is negligible (about 2% of the relative sea level change due to uplift; see Figure S3).

There are two reasons elastic deformation and geoid perturbations are less important to ice-sheet stability here than in Gomez et al. (2015) or Larour et al. (2019). First, the mass loss we consider is significantly smaller, concentrated around the evolving grounding line of Pine Island rather than the whole of Antarctica. Second, the upper mantle viscosity we consider here (10^{18}-10^{19} Pa s) is an order-of-magnitude less than in Gomez et al. (2015) (10^{19}-10^{20} Pa s). The solid-Earth response is sufficiently rapid in UB that the surface is kept close to gravitational equilibrium and ice mass lost is balanced almost immediately by rising mantle material, which results in more uplift than elastic rebound alone. This is true also for slightly slower responses (such as "Best2"): the gravitational effect on relative sea level is slightly larger, but still less than 6% of that due to GIA-related deformations (see Figure S3g and j). We conclude that, for this region, viscoelastic uplift is far more locally stabilizing for local mass losses than either gravitational or purely elastic effects for a low viscosity mantle.

4.2 Uplift from past ice mass changes

Here, we have only considered uplift from mass lost after the start of the simulation. The volume of ice has fluctuated on millennial timescales (Kingslake et al., 2018) and observations record ongoing mass loss for several decades (Rignot et al., 2019), so there is background uplift already occurring in the region. We could compute this uplift either by modeling the past ice mass changes or by inverting observations of bedrock velocities. As indicated by Figure 3(g), however, the features of the velocity field are highly localized to the grounding line and observations (black dots in 3g) have yet to resolve vertical velocities on this small scale. Furthermore, modeling by Barletta et al. (2018) shows that the present-day uplift rates are insensitive to ice mass changes since the last glacial maximum and only slightly more sensitive to the rate of ice mass loss over the last century.

We demonstrate that the amount of remaining uplift from the rate of recent local melt is negligible compared to contemporaneous uplift-rate for the UB model with an order-of-magnitude experiment. The viscoelastic uplift remaining to equilibrium Δu after t years of constant, stationary ice thinning with velocity $v(> 0)$ reaches a steady state if its duration t is long, compared with a characteristic relaxation time ($t \gg \tau$), as the viscoelastic uplift rate comes to match the rate of mass loss not supported by the elastic lithosphere:

$$\Delta u = \rho_i g T v \tau, \tag{9}$$

where ρ_i is the density of ice, and the other symbols have been defined above (see text S2 for a complete derivation). Between 1992 and 2011 the grounding line at Pine Island Glacier retreated 31 km at its center (Rignot et al., 2014) and thinned at a rate of about 4 m/yr (Thomas et al., 2004). The 19-year duration of this mass loss (Rignot et al., 2014) is much longer than the GIA timescale for loads at the scale of the grounding line (10s of km, $\tau \sim 10^{-1}$ yr, see Figure 1b), which justifies our steady-state assumption. Using the simplifying assumptions that the mass loss is constant and occurs in a 31 km $\times$ 31 km box centered on the grounding line, and ignoring mass changes in adjacent systems, we get an order of magnitude for the remaining viscoelastic uplift near the grounding line of about 1.1 m (and velocity 60 mm/yr) for the UB model and 0.8 m (20 mm/yr) for Best2 (see Figure S4b-f), which is smaller than the uncertainty in the bed topography (Fretwell et al., 2013). Initializing the uplift field with this mass loss results in only slightly more stability for model UB (see Figure S5).

Recent melt dominates the uplift signal because of the fast relaxation time of the local viscous structure, and we achieve an approximate match of the present-day GPS vertical uplift rates at the two stations nearest Pine Island Glacier using the rough mass loss described above (Figure S4b) with a thin lithosphere. Fitting those observations with a thicker lithosphere (Figure S4c-d) would require modeling older mass changes.

4.3 Effects of bedrock geometry and melt parameterization

A final source of variation for the stability associated with viscoelastic uplift is the uncertainty in the driving forces for mass loss, e.g. the bedrock geometry, sub-ice shelf melt rates, sliding laws, surface mass balance, etc. For example, a ridge in front of the grounding line may be an artifact of observational data processing (Rignot et al., 2014; Nias et al., 2016). The decreased buttressing from removing this ridge allows the grounding line to retreat much more rapidly in the initial stages, outpacing the uplift and reducing its stabilizing influence (to about 15%, Figure S5). Doubling the basal melt rate has the same effect.

This suggests an important interplay between the rate and location of mass loss, the speed of the bed response, and the ocean forcing. We also do not consider the bed response to mass changes outside the domain, which would superimpose on the response modeled here, causing either uplift or subsidence. Any local mass loss causes uplift that decreases water depth at the grounding line and slows retreat, as thickness is a first-order control on the rate of ice flow across the grounding line. However, uplift centered ahead of the grounding line could increase the slope of the retrograde bed enough to leave it more vulnerable to instability from future changes in grounding line flux. For local losses from Pine Island, the space- and time- scale of uplift could be comparable enough to the decadal trend of melt-driven grounding line retreat to slow it. For similar, vulnerable glaciers, such as Thwaites Glacier nearby, details of this interplay are crucial for predicting the impacts of collapse and might require resolving GIA on scales larger than are appropriate for the flat-earth approximation employed here.

5 Conclusion

We demonstrated the potential importance of rapid viscoelastic GIA-related deformations in dynamically slowing the decadal grounding line retreat of Pine Island Glacier by coupling a dynamic ice flow model to a viscoelastically deforming half-space. The magnitude of the feedback depends upon the ability of the mantle response to keep pace with the rate of mass lost. For the rapid retreat of Pine Island Glacier, simulated here by increased sub-ice shelf melting, uplift slows the rate of mass lost by between 10 and 30% over 150 years, relative to scenarios with no bed deformation. The upper limit is based on a weak-end-member mantle rheology that is broadly consistent with geophysical observations from this and other regions. These findings are consistent with previous theoretical (Gomez et al., 2015) and observational (Kingslake et al., 2018; Barletta et al., 2018) work, although on shorter time scales owing to the regionally low viscosity and high-resolution coupling used here. Considering only losses at Pine Island, other components of GIA, such as perturbations to the geoid and existing uplift from previous mass loss, have a further (although smaller) impact (Gomez et al., 2010, 2015; Larour et al., 2019) on retreat. This work highlights the importance of coupling GIA-related deformations when predicting the grounding line evolution of marine ice sheets, particularly in regions characterized by large lateral heterogeneities, and the requirement of high-resolution, local constraints on mantle rheology and bedrock topography over time.

Code and Data Availability

We used the GIANT-BISICLES branch of the publicly available version of the BISICLES ice sheet model code, release version 1.0. Instructions for downloading and installing BISICLES may be found in the "getting started" section at `http://bisicles.lbl.gov`. The specific svn command for obtaining the relevant branch after free registration with ANAG (`https://anag-repo.lbl.gov/`) is:

```
svn co https://anag-repo.lbl.gov/svn/BISICLES/public/branches/GIANT-BISICLES
BISICLES
```

BISICLES is written in a combination of C++ and FORTRAN and is built upon the Chombo AMR software framework. More information about Chombo may be found at `http://Chombo.lbl.gov`.

Static code, data, input, and configuration files for the runs in this work are available at

`https://portal.nersc.gov/cfs/iceocean/GIAPineIsland`

All maps are projected on Polar Stereographic with a standard latitude of -71 degrees, the WGS84 ellipsoid, and origin (-384 km Easting, 1707 km Northing).

Acknowledgments

Support for this work was provided through the Scientific Discovery through Advanced Computing (SciDAC) program funded by the US Department of Energy (DOE), Office of Science, Biological and Environmental Research, and Advanced Scientific Computing Research programs. Work at the University of Michigan was supported under NSFPLR-NERC grant No. 1738896, as part of the International Thwaites Glacier Collaboration's (ITGC) DOMINOS project. Work at LBL was supported by the Director, Office of Science, Offices of Advanced Scientific Computing Research (ASCR) and Biological and Environmental Research (BER), of the U.S. Department of Energy under Contract No. DE-AC02-05CH11231, as a part of the ProSPect SciDAC Partnership. This research used resources of the National Energy Research Scientific Computing Center, a DOE Office of Science user facility supported by the Office of Science of the US Department of Energy under contract no. DE-AC02-05CH11231. We thank the editor, Mathieu Morlighem, Pippa Whitehouse, and an anonymous reviewer for many constructive comments.

References

Adhikari, S., Ivins, E. R., Larour, E., Seroussi, H., Morlighem, M., & Nowicki, S. (2014). Future Antarctic bed topography and its implications for ice sheet dynamics. *Solid Earth*, *5*(1), 569–584. doi: 10.5194/se-5-569-2014

An, M., Wiens, D. A., Zhao, Y., Feng, M., Nyblade, A. A., Kanao, M., . . . Lévêque, J.-J. (2015). S-velocity model and inferred Moho topography beneath the Antarctic Plate from Rayleigh waves. *Journal of Geophysical Research: Solid Earth*, *120*(1), 359–383. Retrieved from `https://agupubs.onlinelibrary.wiley.com/doi/abs/10.1002/2014JB011332` doi: 10.1002/2014JB011332

Auriac, A., Spaans, K. H., Sigmundsson, F., Hooper, A., Schmidt, P., & Lund, B. (2013). Iceland rising : Solid Earth response to ice retreat inferred from satellite radar interferometry and visocelastic modeling. *Journal of*

Geophysical Research: Solid Earth, *118*(December 2012), 1331–1344. doi: 10.1002/jgrb.50082

Bamber, J. L., & Dawson, G. J. (2020). Complex evolving patterns of mass loss from Antarctica's largest glacier. *Nature Geoscience*, *13*(February). Retrieved from http://dx.doi.org/10.1038/s41561-019-0527-z doi: 10.1038/s41561-019-0527-z

Barletta, V. R., Bevis, M., Smith, B. E., Wilson, T., Brown, A., Bordoni, A., ... Wiens, D. A. (2018). Observed rapid bedrock uplift in Amundsen Sea Embayment promotes ice-sheet stability. *Science*, *1339*(June), 1335–1339. doi: 10.1126/science.aao1447

Bueler, E., Lingle, C. S., & Kallen-Brown, J. a. (2007). Fast computation of a viscoelastic deformable Earth model for ice sheet simulation. *Ann. Glaciol.*, *46*, 97–105. doi: 10.3189/172756407782871567

Caron, L., Ivins, E. R., Larour, E., Adhikari, S., Nilsson, J., & Blewitt, G. (2018). GIA Model Statistics for GRACE Hydrology, Cryosphere, and Ocean Science. *Geophysical Research Letters*, *45*, 1–10.

Cathles, L. (1975). *The Viscosity of the Earth's Mantle.* Princeton, NJ: Princeton University Press.

Cornford, S. L., Martin, D. F., Graves, D. T., Ranken, D. F., Le Brocq, A. M., Gladstone, R. M., ... Lipscomb, W. H. (2013). Adaptive mesh , finite volume modeling of marine ice sheets. *Journal of Computational Physics*, *232*(1), 529–549. Retrieved from http://dx.doi.org/10.1016/j.jcp.2012.08.037 doi: 10.1016/j.jcp.2012.08.037

Cornford, S. L., Martin, D. F., Lee, V., Payne, A. J., & Ng, E. G. (2016). Adaptive mesh refinement versus subgrid friction interpolation in simulations of Antarctic ice dynamics. *Annals of Glaciology*, *57*(73), 1–9. doi: 10.1017/aog.2016.13

Cornford, S. L., Martin, D. F., Payne, A. J., Ng, E. G., Le Brocq, A. M., Gladstone, R. M., ... Vaughan, D. G. (2015). Century-scale simulations of the response of the West Antarctic Ice Sheet to a warming climate. *Cryosphere*, *9*(4), 1579–1600. doi: 10.5194/tc-9-1579-2015

Dziewonski, A. M., & Anderson, D. L. (1981, 6). Preliminary reference Earth model. *Physics of the Earth and Planetary Interiors*, *25*(4), 297–356. Retrieved from http://linkinghub.elsevier.com/retrieve/pii/0031920181900467 doi:

10.1016/0031-9201(81)90046-7

Favier, L., Durand, G., Cornford, S. L., Gudmundsson, G. H., Gagliardini, O., Gillet-Chaulet, F., ... Le Brocq, A. M. (2014). Retreat of Pine Island Glacier controlled by marine ice-sheet instability. *Nature Climate Change*, *4*(2), 117–121. Retrieved from http://dx.doi.org/10.1038/nclimate2094 doi: 10.1038/nclimate2094

Fjeldskaar, W. (1991). Geoidal-eustatic changes induced by the deglaciation of Fennoscandia. *Quaternary International*, *9*(C), 1–6. doi: 10.1016/1040-6182(91)90058-V

Fretwell, P., Pritchard, H. D., Vaughan, D. G., Bamber, J. L., Barrand, N. E., Bell, R., ... Zirizzotti, A. (2013). Bedmap2: Improved ice bed, surface and thickness datasets for Antarctica. *Cryosphere*, *7*(1), 375–393. doi: 10.5194/tc-7-375-2013

Gomez, N., Latychev, K., & Pollard, D. (2018). A Coupled Ice Sheet – Sea Level Model Incorporating 3D Earth Structure : Variations in Antarctica during the Last Deglacial Retreat. *Journal of Climate*, *31*, 4041–4054. doi: 10.1175/JCLI-D-17-0352.1

Gomez, N., Mitrovica, J. X., Huybers, P., & Clark, P. U. (2010). Sea level as a stabilizing factor for marine-ice-sheet grounding lines. *Nature Geoscience*, *3*(12), 850–853. doi: 10.1038/ngeo1012

Gomez, N., Pollard, D., & Holland, D. (2015). Sea-level feedback lowers projections of future Antarctic Ice-Sheet mass loss. *Nature Communications*, *6*, 1–8. Retrieved from http://dx.doi.org/10.1038/ncomms9798 doi: 10.1038/ncomms9798

Gomez, N., Pollard, D., Mitrovica, J. X., Huybers, P., & Clark, P. U. (2012). Evolution of a coupled marine ice sheet-sea level model. *Journal of Geophysical Research: Earth Surface*, *117*(1), 1–9. doi: 10.1029/2011JF002128

Gudmundsson, G. H. (2013). Ice-shelf buttressing and the stability of marine ice sheets. *Cryosphere*, *7*(2), 647–655. doi: 10.5194/tc-7-647-2013

Hay, C. C., Lau, H. C., Gomez, N., Austermann, J., Powell, E., Mitrovica, J. X., ... Wiens, D. A. (2017). Sea level fingerprints in a region of complex earth structure: The case of WAIS. *Journal of Climate*, *30*(6), 1881–1892. doi: 10.1175/JCLI-D-16-0388.1

Huybrechts, P. (2002, 1). Sea-level changes at the LGM from ice-dynamic reconstructions of the Greenland and Antarctic ice sheets during the glacial cycles. *Quaternary Science Reviews*, *21*(1-3), 203–231. Retrieved from http://linkinghub.elsevier.com/retrieve/pii/S0277379101000828 doi: 10.1016/S0277-3791(01)00082-8

Ivins, E. R., James, T. S., Wahr, J., Ernst, E. J., Landerer, F. W., & Simon, K. M. (2013). Antarctic contribution to sea level rise observed by GRACE with improved GIA correction. *Journal of Geophysical Research: Solid Earth*, *118*(6). doi: 10.1002/jgrb.50208

Joughin, I., Smith, B. E., & Medley, B. (2014). Marine Ice Sheet Collapse Potentially Under Way for the Thwaites Glacier Basin, West Antarctica. *Science*, *344*(May), 735–739.

Joughin, I., Tulaczyk, S., Bamber, J. L., Blankenship, D., Holt, J. W., Scambos, T., & Vaughan, D. G. (2009). Basal conditions for Pine Island and Thwaites Glaciers, West Antarctica, determined using satellite and airborne data. *Journal of Glaciology*, *55*(190), 245–257. doi: 10.3189/002214309788608705

Kachuck, S. B., & Cathles, L. (2019). Benchmarked computation of time-domain viscoelastic Love numbers for adiabatic mantles. *Geophysical Journal International*. doi: 10.1093/gji/ggz276

Kingslake, J., Scherer, R. P., Albrecht, T., Coenen, J., Powell, R. D., Reese, R., … Whitehouse, P. L. (2018). Extensive retreat and re-advance of the West Antarctic Ice Sheet during the Holocene. *Nature*, 0–1. Retrieved from http://dx.doi.org/10.1038/s41586-018-0208-x doi: 10.1038/s41586-018-0208-x

Klemann, V., Wu, P., & Wolf, D. (2003). Compressible viscoelasticity : stability of solutions for homogeneous plane-Earth models. *Geophys. J. Int.*, *153*(November), 569–585.

Konrad, H., Sasgen, I., Pollard, D., & Klemann, V. (2015). Potential of the solid-Earth response for limiting long-term West Antarctic Ice Sheet retreat in a warming climate. *Earth and Planetary Science Letters*, *432*, 254–264. Retrieved from http://dx.doi.org/10.1016/j.epsl.2015.10.008 doi: 10.1016/j.epsl.2015.10.008

Lange, H., Casassa, G., Ivins, E. R., Schröder, L., Fritsche, M., Richter, A., … Dietrich, R. (2014). Observed crustal uplift near the Southern Patagonian Icefield constrains improved viscoelastic Earth models. *Geophysical Research Letters*, *41*(3), 805–812. doi: 10.1002/2013GL058419

Larour, E., Seroussi, H., Adhikari, S., Ivins, E., Caron, L., Morlighem, M., & Schlegel, N. (2019). Slowdown in Antarctic mass loss from solid Earth and sea-level feedbacks. *Science*(April), eaav7908. Retrieved from http://www.sciencemag.org/lookup/doi/10.1126/science.aav7908 doi: 10.1126/science.aav7908

Larsen, C. F., Motyka, R. J., Freymueller, J. T., Echelmeyer, K. A., & Ivins, E. R. (2005, 9). Rapid viscoelastic uplift in southeast Alaska caused by post-Little Ice Age glacial retreat. *Earth and Planetary Science Letters*, *237*(3-4), 548–560. Retrieved from http://www.sciencedirect.com/science/article/pii/S0012821X05004152 doi: 10.1016/j.epsl.2005.06.032

Le Muir, E., & Huybrechts, P. (1996). A comparison of different ways of dealing with isostasy: examples from modelling the Antarctic ice sheet during the last glacial cycle. *Annals of glaciology*, *23*, 309–317. Retrieved from http://www.sciencedirect.com/science/article/pii/S0277379113003338%5Cnhttp://dx.doi.org/10.1038/ngeo411%5Cnhttp://www.sciencedirect.com/science/article/pii/B044452747800346X%5Cnhttps://sites.google.com/site/mnamaris/%5Cnhttp://adsabs.harvard.edu/abs/1959J doi: 10.3189/S0260305500013586

Lingle, C. S., & Clark, J. A. (1985). A numerical model of interactions between a marine ice sheet and the solid earth: Application to a West Antarctic ice stream. *Journal of Geophysical Research*, *90*(C1), 1100. Retrieved from http://doi.wiley.com/10.1029/JC090iC01p01100 doi: 10.1029/JC090iC01p01100

Martin, D. F., Cornford, S. L., & Payne, A. J. (2019). Millennial-Scale Vulnerability of the Antarctic Ice Sheet to Regional Ice Shelf Collapse. *Geophysical Research Letters*, *46*(3), 1467–1475. doi: 10.1029/2018GL081229

Medley, B., Joughin, I., Smith, B. E., Das, S. B., Steig, E. J., Conway, H., ... Leuschen, C. (2014). Constraining the recent mass balance of Pine Island and Thwaites glaciers, West Antarctica, with airborne observations of snow accumulation. *Cryosphere*, *8*(4), 1375–1392. doi: 10.5194/tc-8-1375-2014

Mitrovica, J. X., & Forte, A. M. (1997). Radial profile of mantle viscosity : Results from the joint inversion of convection and postglacial rebound observables. *Journal of Geophysical Research*, *102*, 2751–2769. Retrieved from `http://www.agu.org/pubs/crossref/1997/96JB03175.shtml`

Nias, I. J., Cornford, S. L., & Payne, A. J. (2016). Contrasting the Modelled sensitivity of the Amundsen Sea Embayment ice streams. *Journal of Glaciology*, *62*(233), 552–562. doi: 10.1017/jog.2016.40

Nield, G. A., Barletta, V. R., Bordoni, A., King, M. A., Whitehouse, P. L., Clarke, P. J., . . . Berthier, E. (2014). Rapid bedrock uplift in the Antarctic Peninsula explained by viscoelastic response to recent ice unloading. *Earth and Planetary Science Letters*, *397*, 32–41. Retrieved from `http://dx.doi.org/10.1016/j.epsl.2014.04.019` doi: 10.1016/j.epsl.2014.04.019

Pattyn, F. (2018). The paradigm shift in Antarctic ice sheet modelling. *Nature Communications*, *9*(1), 10–12. Retrieved from `http://dx.doi.org/10.1038/s41467-018-05003-z` doi: 10.1038/s41467-018-05003-z

Pollard, D., Gomez, N., & Deconto, R. M. (2017). Variations of the Antarctic Ice Sheet in a Coupled Ice Sheet-Earth-Sea Level Model: Sensitivity to Viscoelastic Earth Properties. *Journal of Geophysical Research: Earth Surface*, *122*(11), 2124–2138. doi: 10.1002/2017JF004371

Purcell, A. P. (1998). The significance of pre-stress advection and internal buoyancy in the flat-Earth formulation. In P. Wu (Ed.), *Dynamics of the ice age earth: a modern perspective* (pp. 105–122). Trans. Tech. Publications, Hetikon.

Ramirez, C., Nyblade, A., Hansen, S. E., Wiens, D. A., Anandakrishnan, S., Aster, R. C., . . . Wilson, T. (2016). Crustal and upper-mantle structure beneath ice-covered regions in Antarctica from S-wave receiver functions and implications for. *Geophysical Journal International*, *204*, 1636–1648. doi: 10.1093/gji/ggv542

Rignot, E., Bamber, J. L., van den Broeke, M. R., Davis, C., Li, Y., van de Berg, W. J., & van Meijgaard, E. (2008, 1). Recent Antarctic ice mass loss from radar interferometry and regional climate modelling. *Nature Geoscience*, *1*(2), 106–110. Retrieved from `http://www.nature.com/doifinder/10.1038/ngeo102` doi: 10.1038/ngeo102

Rignot, E., Mouginot, J., Morlighem, M., Seroussi, H., & Scheuchl, B. (2014).

Widespread, rapid grounding line retreat of Pine Island, Thwaites, Smith, and Kohler glaciers, West Antarctica, from 1992 to 2011. *Geophysical Research Letters*, *41*(10), 3502–3509. doi: 10.1002/2014GL060140

Rignot, E., Mouginot, J., Scheuchl, B., van den Broeke, M. R., van Wessem, M. J., & Morlighem, M. (2019). Four decades of Antarctic Ice Sheet mass balance from 1979-2017. *Proceedings of the National Academy of Sciences*, 1–9. doi: 10.1073/pnas.1812883116

Schoof, C. (2007). Ice sheet grounding line dynamics: Steady states, stability, and hysteresis. *Journal of Geophysical Research: Earth Surface*, *112*(3), 1–19. doi: 10.1029/2006JF000664

Schoof, C. (2012). Marine ice sheet stability. *Journal of Fluid Mechanics*, *698*, 62–72. Retrieved from `http://www.eos.ubc.ca/~cschoof/marinestability.pdf`

Simms, A. R., Ivins, E. R., DeWitt, R., Kouremenos, P., & Simkins, L. M. (2012). Timing of the most recent Neoglacial advance and retreat in the South Shetland Islands, Antarctic Peninsula: Insights from raised beaches and Holocene uplift rates. *Quaternary Science Reviews*, *47*, 41–55. Retrieved from `http://dx.doi.org/10.1016/j.quascirev.2012.05.013` doi: 10.1016/j.quascirev.2012.05.013

Spada, G. (2003). The theory behind TABOO. *Samizdat, Golden, Colo.*

Thomas, R., Rignot, E., Casassa, G., Kanagaratnam, P., Acuña, C., Akins, T., ... Zwally, J. (2004). Accelerated sea-level rise from west Antarctica. *Science*, *306*(5694), 255–258. doi: 10.1126/science.1099650

Vermeersen, L. L., & Sabadini, R. (1997). A new class of stratified viscoelastic models by analytical techniques. *Geophysical Journal International*, *129*(3), 531–570. doi: 10.1111/j.1365-246X.1997.tb04492.x

Waibel, M. S., Hulbe, C. L., Jackson, C. S., & Martin, D. F. (2018). Rate of Mass Loss Across the Instability Threshold for Thwaites Glacier Determines Rate of Mass Loss for Entire Basin. *Geophysical Research Letters*, *45*(2), 809–816. doi: 10.1002/2017GL076470

Weertman, J. (1974). Stability of the Junction of an Ice Sheet and an Ice Shelf. *Journal of Glaciology*, *13*(67), 3–11. Retrieved from `https://www.cambridge.org/core/product/identifier/S0022143000023327/type/`

journal_article doi: 10.3189/S0022143000023327

Whitehouse, P. L., Gomez, N., King, M. A., & Wiens, D. A. (2019). Solid Earth change and the evolution of the Antarctic Ice Sheet. *Nature Communications*, *10*(1), 1–14. Retrieved from http://dx.doi.org/10.1038/s41467-018-08068-y doi: 10.1038/s41467-018-08068-y

Wolf, D. (1984). The relaxation of spherical and flat Maxwell Earth models and effects due to the presence of the lithosphere. *Journal of Geophysics*, *56*(1), 24–33.

Wolf, D. (1985). The normal modes of a layered, incompressible Maxwell half-space. *Journal of Geophysics - Zeitschrift fur Geophysik*, *57*(2), 106–117.

Wolf, D. (1998). Load-Induced Viscoelastic Relaxation: An Elementary Example. In P. Wu (Ed.), *Dynamics of the ice age earth: a modern perspective* (pp. 87–104). Trans. Tech. Publications, Hetikon.

Yuen, D. a., & Peltier, W. R. (1982). Normal modes of the viscoelastic earth. *Geophys. J. R. astr. Soc.*, *69*, 495–526. doi: 10.1111/j.1365-246X.1982.tb04962.x

Zwally, H. J., Giovinetto, M. B., Beckley, M. A., & Saba, J. L. (2012). Antarctic and Greenland drainage systems, GSFC cryospheric sciences laboratory. *Available at icesat4. gsfc. nasa. gov/cryo_data/ant_grn_drainage_systems. php. Accessed March*, *1*, 2015.

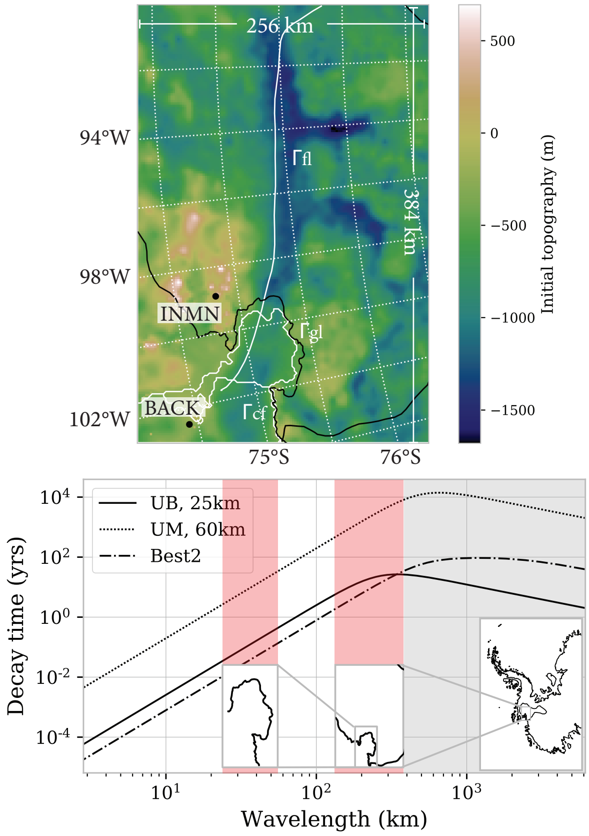

Figure 1. a) The computational domain for Pine Island Glacier with initial topography from Bedmap2 (Fretwell et al., 2013). The fixed calving front (Γ_{cf}), initial grounding line (Γ_{gl}), and a flowline used for transects (Γ_{fl}) are shown in white with the catchment basin (black, from Zwally et al., 2012). b) The relaxation decay times for harmonic loads as a function of wavelength for the average upper mantle (UM; 10^{21} Pa s, 60 km Lithosphere; dotted), a low viscosity, Upper Bound (UB) model (solid), and "Best2" from Barletta et al. (2018) (dash-dot). Inset maps and shaded regions indicate approximate spatial scale of loads typical for the grounding line (red, left) and problem domain (red, right). The grey shaded region shows continental-scale loads, which are not considered.

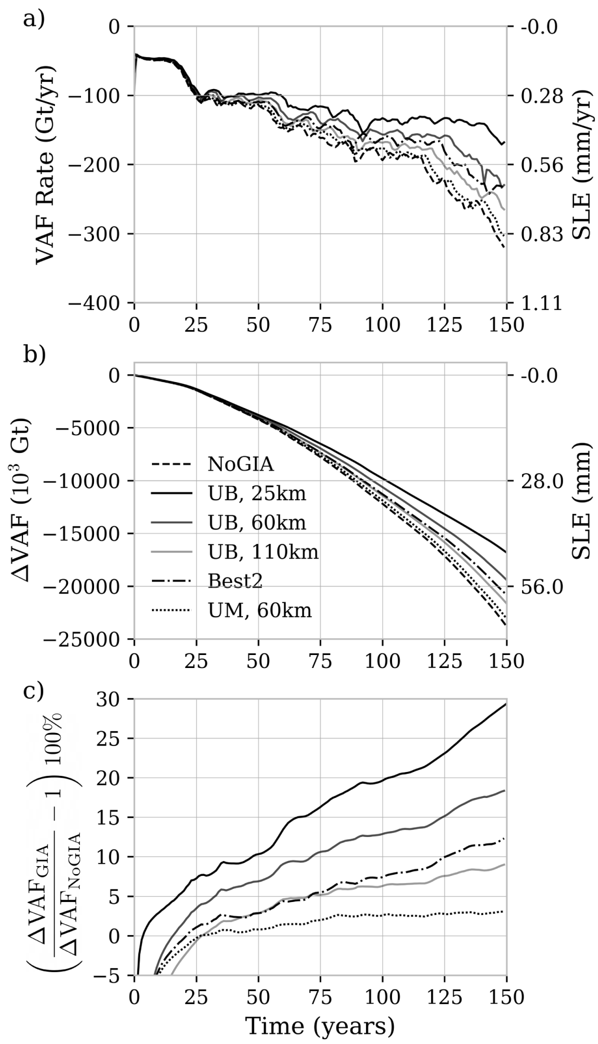

Figure 2. Results from coupling Pine Island Glacier flow to GIA-related deformation over 150 years for different rheologies: static bedrock (NoGIA, dashed), the Upper Bound coupling case of a 10^{18} Pa s half-space (UB, solid) overlain by 25 km, 60 km, and 110 km lithospheres (dark to light), the "Best2" model (Best2, dash-dot), and the upper mantle average viscosity of 10^{21} Pa s with 60 km lithosphere (UM, dotted). a) Volume above flotation (VAF) loss rate in Gigatons of ice and millimeters of equivalent sea level rise (SLE). b) Change in total VAF (ΔVAF) relative to $t = 0$. c) Percentage difference ΔVAF (from b) between models with GIA-related deformation relative to without. Instantaneous elastic subsidence at the grounding line increases mass loss initially, but is soon overtaken by viscoelastic uplift in response to overall mass loss. The low-viscosity, thin lithosphere mantle reduces projected mass loss significantly over decadal to centennial timescales.

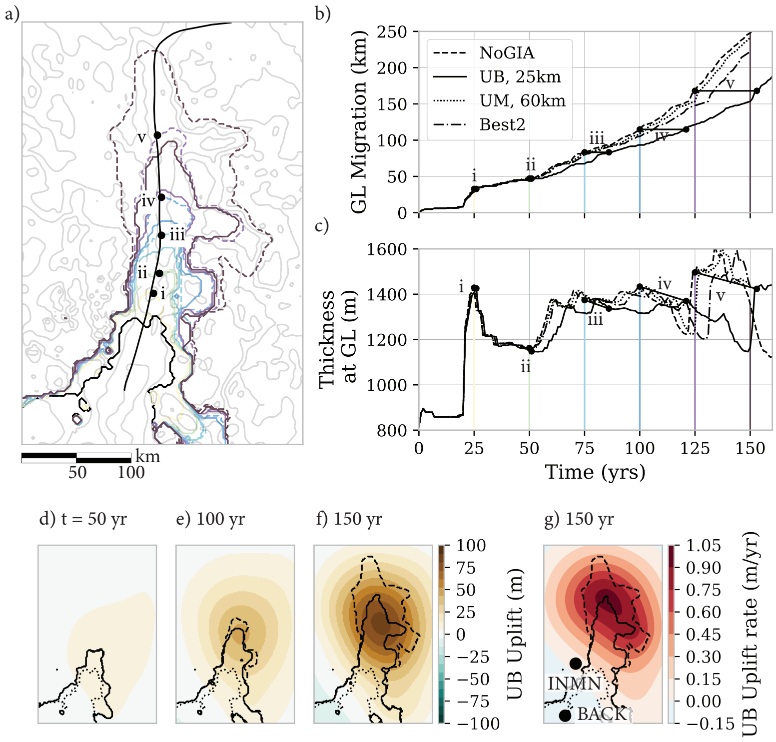

Figure 3. Viscoelastic uplift of the grounding line (GL) slows retreat. a) GL location every 25 years over the 150 year simulation without (dashed) and with (solid) viscoelastic coupling. The uncoupled GL's distance along a center flowline has been marked by five points (i-v). Bathymetry (grey contours) shown. (b-c) Difference in GL retreat along the flowline by distance (b) and thickness of ice (c), which is proportional to uplift at the GL for models NoGIA (dashed), UB (solid), "Best2" (dash-dot), and UM (dotted). Points i-v along the retreat are marked to show the delay in retreat (over 25 years by 150 years) caused by uplift (65 m) between models NoGIA and UB. d-f) The regional uplift at three times: t=50, 100, and 150 years for model UB, with the initial GL (dotted) and predicted GL (UB-solid, NoGIA-dashed) contours shown. The maximum uplift is predicted just in front of the grounding line. g) The uplift rate predicted at t=150 years for model UB, with the maximum just behind the GL, where thinning is most pronounced. Nearby labeled GPS observations from Barletta et al. (2018) lie outside the region of maximum predicted uplift.

Figure 1.

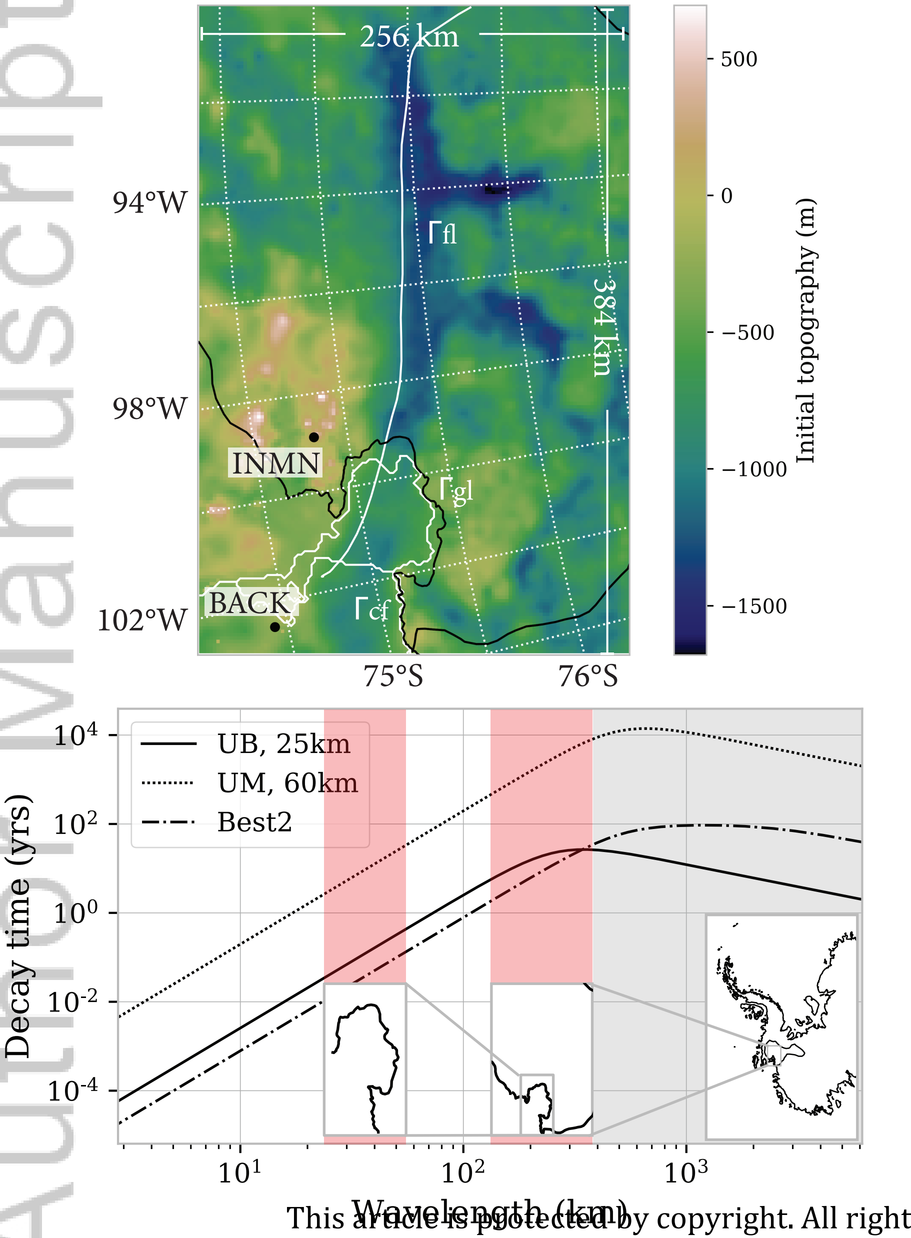

256 km
384 km
94°W
98°W
102°W
75°S
76°S
Γ_{fl}
Γ_{gl}
Γ_{cf}
INMN
BACK
500
0
−500
−1000
−1500
Initial topography (m)
UB, 25km
UM, 60km
Best2
10^4
10^2
10^0
10^{-2}
10^{-4}
Decay time (yrs)
10^1
10^2
10^3
Wavelength (km)

Figure 2.

a)
VAF Rate (Gt/yr)
SLE (mm/yr)
0
−100
−200
−300
−400
-0.0
0.28
0.56
0.83
1.11
0
25
50
75
100
125
150
b)
ΔVAF (10^3 Gt)
SLE (mm)
0
−5000
−10000
−15000
−20000
−25000
-0.0
28.0
56.0
NoGIA
UB, 25km
UB, 60km
UB, 110km
Best2
UM, 60km
c)
$\left(\frac{\Delta \mathrm{VAF}_{\mathrm{GIA}}}{\Delta \mathrm{VAF}_{\mathrm{NoGIA}}} - 1\right) 100\%$
30
25
20
15
10
5
0
−5
Time (years)

Figure 3.

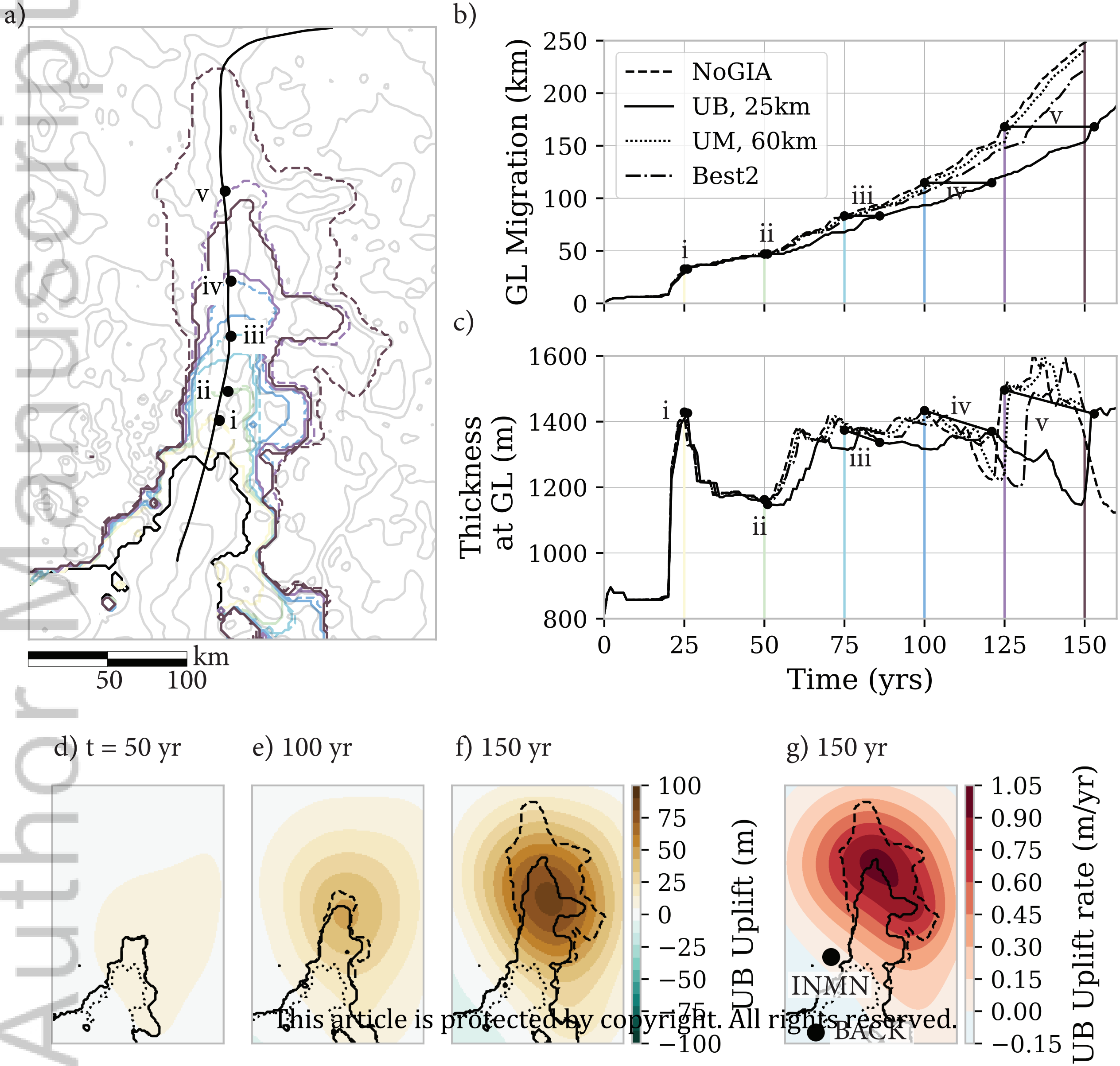
a)
v
iv
iii
ii
i
km
50
100
b)
GL Migration (km)
250
200
150
100
50
0
NoGIA
UB, 25km
UM, 60km
Best2
c)
Thickness at GL (m)
1600
1400
1200
1000
800
0
25
50
75
100
125
150
Time (yrs)
d) t = 50 yr
e) 100 yr
f) 150 yr
g) 150 yr
UB Uplift (m)
100
75
50
25
0
−25
−50
−75
−100
UB Uplift rate (m/yr)
1.05
0.90
0.75
0.60
0.45
0.30
0.15
0.00
−0.15
INMN
BACK

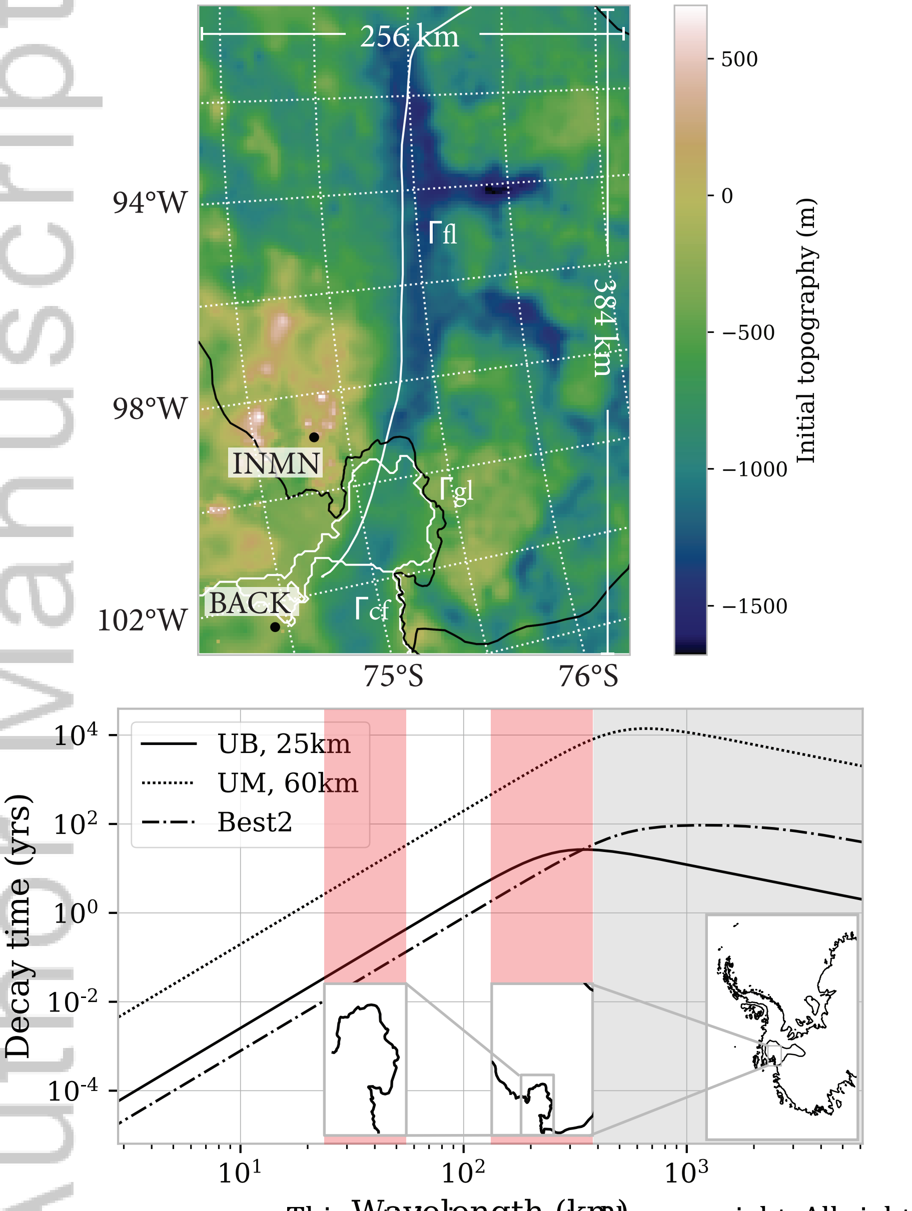
256 km
384 km
94°W
98°W
102°W
75°S
76°S
INMN
BACK
Γfl
Γgl
Γcf
Initial topography (m)
500
0
−500
−1000
−1500
UB, 25km
UM, 60km
Best2
Decay time (yrs)
10^4
10^2
10^0
10^-2
10^-4
10^1
10^2
10^3
Wavelength (km)

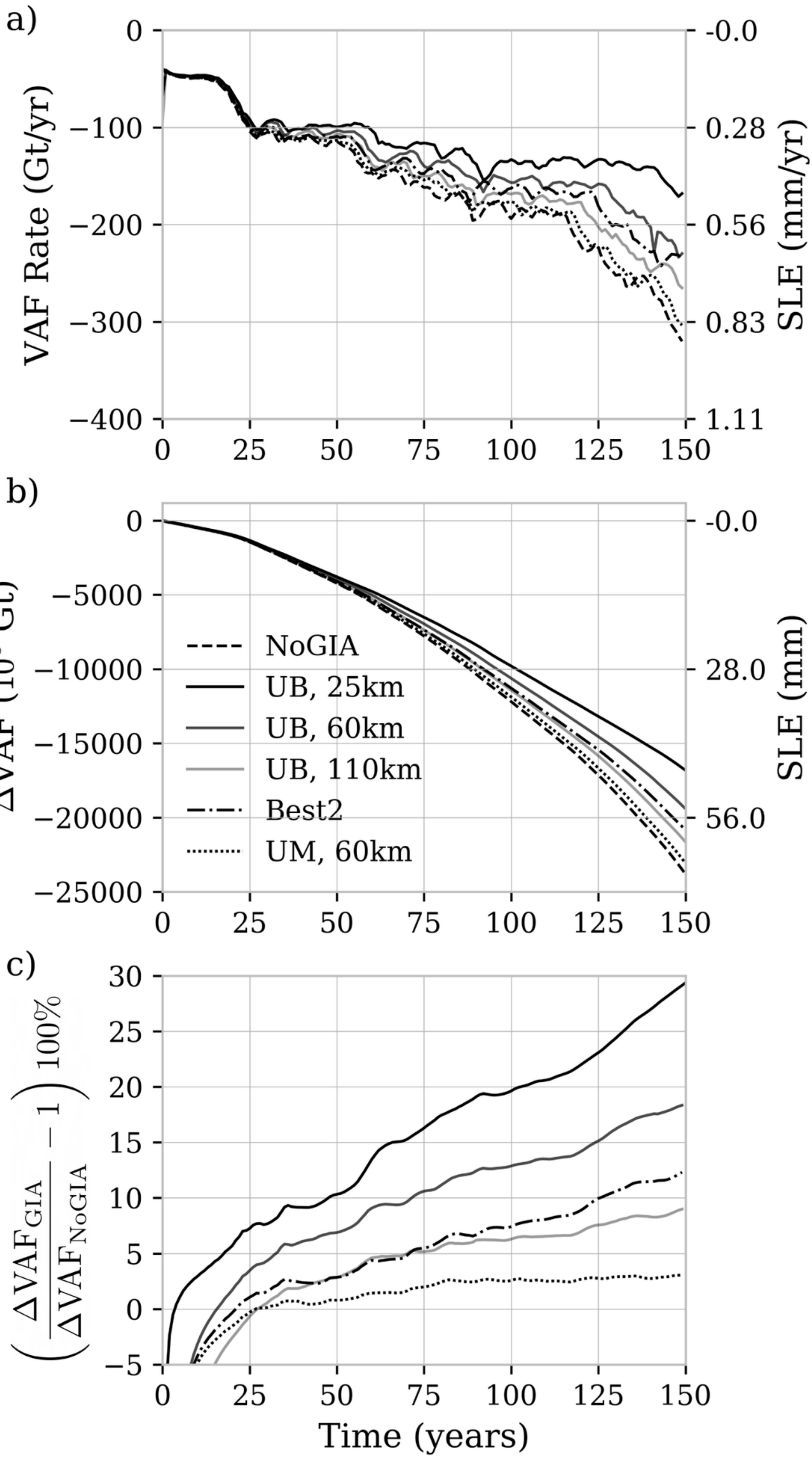

2019GL086446-f02-z-.png

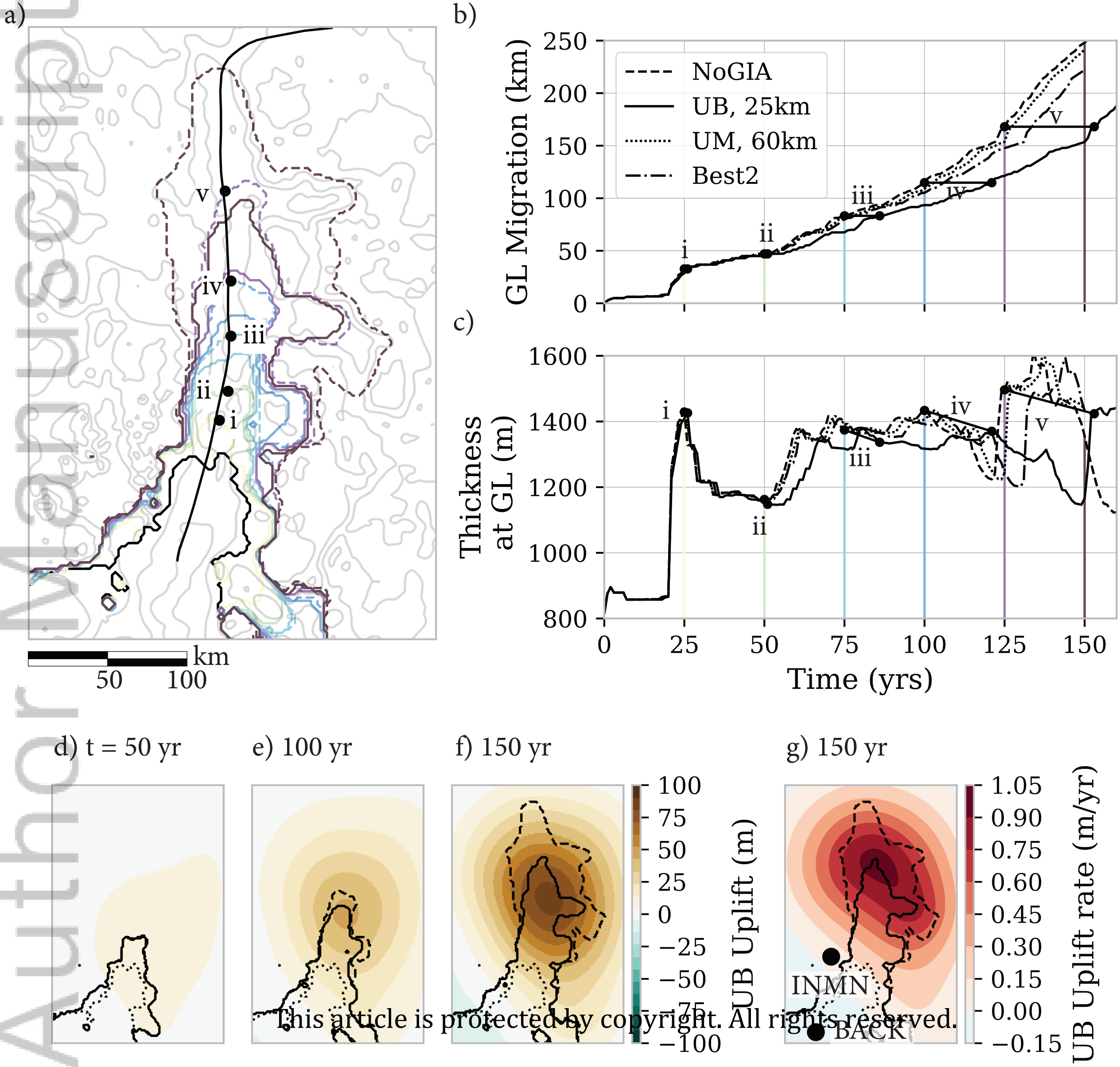

a)
v
iv
iii
ii
i
km
50
100
b)
GL Migration (km)
250
200
150
100
50
0
NoGIA
UB, 25km
UM, 60km
Best2
c)
Thickness at GL (m)
1600
1400
1200
1000
800
0
25
50
75
100
125
150
Time (yrs)
d) t = 50 yr
e) 100 yr
f) 150 yr
g) 150 yr
UB Uplift (m)
100
75
50
25
0
−25
−50
−75
−100
UB Uplift rate (m/yr)
1.05
0.90
0.75
0.60
0.45
0.30
0.15
0.00
−0.15
INMN
BACK